

Penetration properties of resonant magnetic perturbation in EAST Tokamak

Cite as: Phys. Plasmas **26**, 112502 (2019); <https://doi.org/10.1063/1.5116669>

Submitted: 26 June 2019 . Accepted: 09 October 2019 . Published Online: 01 November 2019

H. W. Zhang , Z. W. Ma , W. Zhang , Y. W. Sun , and X. Yang 



[View Online](#)



[Export Citation](#)



[CrossMark](#)



ULVAC

Leading the World with Vacuum Technology

- Vacuum Pumps
- Leak Detectors
- Arc Plasma Deposition
- Thermal Analysis
- RGAs
- Ellipsometers

Penetration properties of resonant magnetic perturbation in EAST Tokamak

Cite as: Phys. Plasmas **26**, 112502 (2019); doi: [10.1063/1.5116669](https://doi.org/10.1063/1.5116669)

Submitted: 26 June 2019 · Accepted: 9 October 2019 ·

Published Online: 1 November 2019



[View Online](#)



[Export Citation](#)



[CrossMark](#)

H. W. Zhang,¹ Z. W. Ma,^{1,a)} W. Zhang,¹ Y. W. Sun,² and X. Yang³

AFFILIATIONS

¹Institute for Fusion Theory and Simulation, Zhejiang University, Hangzhou 310027, China

²Institute of Plasma Physics, Chinese Academy of Sciences, P.O. Box 1126, Hefei 230031, China

³Chongqing Engineering Laboratory for Detection, Control and Integrated System, Chongqing Technology and Business University, Chongqing 400067, China

^{a)}E-mail: zvma@zj.edu.cn

ABSTRACT

Our three-dimensional toroidal magnetohydrodynamics code [CLT (Ci-Liu-Ti, which means magnetohydrodynamics in Chinese)] is upgraded to CLTx in which the simulation domain extends to a scrape-off layer (SOL). Linear simulation results of resonant magnetic perturbation (RMP) for edge-localized-mode mitigation discharge 52340 in EAST Tokamak agree well with those from the MARS-F code. With the presence of the X-point and the SOL, the RMP amplitude and phase shift in the pedestal region, especially for a higher m mode, are largely affected by the resistivity in the SOL. A phase shift of π for resonant harmonics in vacuum and with a plasma response is observed, which is quite different from the $\pi/2$ shift due to the presence of screen current suggested in the previous studies. Simulation results with different resistivities suggest that the amplitude reduction and the phase shift of the resonant harmonics increase with decreasing the resistivity.

Published under license by AIP Publishing. <https://doi.org/10.1063/1.5116669>

I. INTRODUCTION

Resonant magnetic perturbation (RMP) as an effective method to control edge localized mode (ELM)¹ in H-mode discharge² has been well developed during the past decade. RMP systems have been installed in leading Tokamaks worldwide, such as DIII-D,³ JET,⁴ MAST,⁵ ASDEX-U,⁶ KSTAR,⁷ EAST,⁸ etc.

The successful application of RMP in future Tokamaks, such as ITER,⁹ requires a clear understanding of the penetration mechanism of magnetic perturbations with the presence of the plasma response. Numerous studies focusing on RMP have been carried out,^{9–31} including analytical theories, numerical simulations, and experiments. In ideal magnetohydrodynamic (MHD) theory, the mode structure and linear growth rate can be obtained through solving the eigenvalue problem.^{12,13} Several computational codes, like MARS-F,^{14,15} M3D-C1,^{16–18} JOREK,^{19–23} NIMROD,^{24,25} RMHD,³¹ etc., are used to study the plasma response to RMP. Experiments in Tokamaks are designed to investigate the propagation dynamics of RMP^{7,26} and its influence in many aspects, such as edge-localized-mode (ELM) mitigation,^{8,27,28} tearing mode (TM) control,²⁹ and the suppression of runaway electrons in disruptions.³⁰

The applications of RMP in Tokamaks result in magnetic island overlap and stochasticity in the pedestal region.³² With appropriately imposed RMP, ELM suppression or mitigation can be achieved. For

example, Wade *et al.*¹⁶ found that ELM suppression with RMP in DIII-D is related to the co-alignment of three positions that are the locations with the zero perpendicular electron frequency $\omega_{\perp}^e = 0$, an $n = 3$ rational surface (where n is the toroidal mode number) and the top of the pedestal, respectively. Yang *et al.*¹⁴ found that the optimal control of ELM in EAST occurs when the total resonant harmonic including the plasma response is maximum at the last rational surface. (The magnetic flux at the X-point is smoothed to obtain a finite safety factor at the plasma boundary.) Through careful diagnoses of the RMP propagation in KSTAR H-mode discharge, Xiao *et al.*⁷ found that the perturbation field first results in a plasma response at the $q = 3$ surface and then propagates into the $q = 2$ surface, where q is the safety factor.

In the paper, we present linear simulation results of the RMP penetration in EAST using CLTx that is an extended version of the three-dimensional, toroidal, and compressible MHD code CLT (Ci-Liu-Ti, which means magnetohydrodynamics in Chinese).^{33–36} In CLTx, the simulation domain includes both the main plasma discharge region and the scrape-off layer (SOL). For the ELM mitigation discharge 52340 in EAST, linear simulation results from CLTx are in good agreement with those of MARS-F.^{14,37} Due to the presence of the X-point and the SOL in CLTx, the magnetic field perturbation in the SOL is not confined as in closed field lines and can propagate along

opened field lines by shear Alfvén waves. A phase shift of π in vacuum and with a plasma response is observed with a low resistivity. (Note that the magnetic field perturbation with a plasma response in this paper means the total perturbed field including the contributions from both the vacuum RMP field and the plasma response field.) The radial diffusion time of RMP is mainly determined by the resistivity. Therefore, we expect that the amplitude reduction and the phase shift of the resonant harmonics increase with decreasing the resistivity when they reach the plasma boundary or the separatrix, which could be regarded as verification and extension of previous conclusions related to the resistivity.^{23,31} The influences on the amplitude and the phase shift of resonant modes due to losing confinement of magnetic perturbations in the SOL become more pronounced for higher resonant modes.

II. THE SIMULATION MODEL FOR CLTx

In CLTx, we use the same set of single fluid, resistive, full MHD equations including dissipations as in CLT,³³ i.e.,

$$\partial_t \rho = -\nabla \cdot (\rho \mathbf{v}) + \nabla \cdot [D \nabla (\rho - \rho_0)], \quad (1)$$

$$\partial_t p = -\mathbf{v} \cdot \nabla p - \Gamma p \nabla \cdot \mathbf{v} + \nabla \cdot [\kappa \nabla (p - p_0)], \quad (2)$$

$$\partial_t \mathbf{v} = -\mathbf{v} \cdot \nabla \mathbf{v} + (\mathbf{J} \times \mathbf{B} - \nabla p)/\rho + \nabla \cdot [\nu \nabla (\mathbf{v} - \mathbf{v}_0)], \quad (3)$$

$$\partial_t \mathbf{B} = -\nabla \times \mathbf{E}, \quad (4)$$

with

$$\mathbf{E} = -\mathbf{v} \times \mathbf{B} + \eta(\mathbf{J} - \mathbf{J}_0), \quad (5)$$

$$\mathbf{J} = \nabla \times \mathbf{B}, \quad (6)$$

where ρ , p , \mathbf{v} , \mathbf{B} , \mathbf{E} , and \mathbf{J} are the plasma density, thermal pressure, plasma velocity, magnetic field, electric field, and current density, respectively. The subscript “0” denotes the equilibrium quantities. Γ ($=5/3$) is the ratio of specific heat of plasma. All variables are normalized as: $\mathbf{B}/B_{00} \rightarrow \mathbf{B}$, $\mathbf{x}/a \rightarrow \mathbf{x}$, $\rho/\rho_{00} \rightarrow \rho$, $\mathbf{v}/v_A \rightarrow \mathbf{v}$, $t/\tau_A \rightarrow t$, $p/(B_{00}^2/\mu_0) \rightarrow p$, $\mathbf{J}/(B_{00}/\mu_0 a) \rightarrow \mathbf{J}$, $\mathbf{E}/(v_A B_{00}) \rightarrow \mathbf{E}$, and $\eta/(\mu_0 a^2/\tau_A) \rightarrow \eta$, where a is equal to one meter, $v_A = B_{00}/\sqrt{\mu_0 \rho_{00}}$ is the Alfvén speed, and $\tau_A = a/v_A$ is the Alfvén time. B_{00} and ρ_{00} are the initial magnetic field and plasma density at the magnetic axis, respectively. Note that the Hall term³⁶ in generalized Ohm’s law is not included in this work; thus, the diamagnetic drifts due to the two-fluid effect are missing.

With the cylindrical coordinate system (R, ϕ, Z) , the cut-cell method³⁸ is adopted to deal with the outer boundary of the poloidal cross section, which enables CLTx to handle irregular boundaries. The simulation domain in CLTx is extended beyond the last closed magnetic surface to the SOL including the X-point, and is restricted inside the limiter given by EFIT (Equilibrium Fitting code) equilibrium.³⁹ Some modifications are done to make the boundary convex. The SOL is treated with low plasma density and pressure, but a large resistivity.⁴⁰ Due to the Courant-Friedrichs-Lowy (CFL) condition, the low plasma density in the SOL largely reduces the time step. Therefore, an OpenACC-MPI heterogeneous parallel scheme in graphics processing units (GPUs) is applied in CLTx to accelerate the simulation.⁴¹

The normalized parameters used in the simulations are fixed to be $D = 1 \times 10^{-6}$, $\kappa = 5 \times 10^{-5}$, and $\mu = 1 \times 10^{-6}$. The spatial distribution of the time-independent resistivity is determined by the initial normalized plasma temperature T with $\eta = \eta_0 \cdot T^{-3/2}$, where η_0 is the resistivity at the magnetic axis which is usually its minimum due

to the maximum temperature. The plasma parameters (including temperature, density, pressure, etc.) in the SOL are missing in the equilibrium reconstructed from EFIT. These parameter values in the SOL are chosen to be the same as those at the separatrix of the plasma boundary. Consequently, if not specified, the resistivity value in the SOL is also the same as that at the separatrix.

III. LINEAR RESULTS FOR EAST DISCHARGE 52340

A. Equilibrium and RMP setup in CLTx

The RMP system in EAST contains two rows of coils (eight coils in each row), located on the upper (“U”) and low (“L”) half-planes indicated by the black bars in Fig. 2. Each coil contains four turns with electric current up to 2.5 kA for each turn. By adjusting the current direction in each coil, the dominant toroidal mode number of RMP could vary from $n = 1$ to 4.⁴² The relative phase difference⁴² between the upper and low coils is defined as $\Delta\Phi = \Phi_U - \Phi_L$. Changing $\Delta\Phi$ results in significant differences in amplitudes of resonant harmonics at rational surfaces, which affects the efficiency of ELM suppression or mitigation by RMP after the plasma response is considered.^{14,37,42} More detailed information about the RMP system in EAST can be found in Refs. 14, 37, and 43.

The initial equilibrium is reconstructed from EAST ELM mitigation discharge 52340 at 3150 ms by EFIT.¹⁴ The initial profiles of safety factor q and the toroidal rotation ω_t are given in Fig. 1. The toroidal rotation profile is the same as that used in previous research by MARS-F.¹⁴ The distribution of the radial component of vacuum RMP b'_{RMP} [10 kAt (kilo-Amp-turns), $n = 1$, $\Delta\Phi = 0$] in the SOL is given in Fig. 2(a). The vacuum RMP field produced by coils is calculated with the Biot-Savart law. The magnetic vector potential \mathbf{A} is used as an intermediate variable in the calculation to guarantee divergence-free of the RMP field. At the initial stage, the magnetic vector potential is assumed to be screened by plasma, which means that the RMP field fills the SOL but rapidly decreases to zero before reaching the plasma boundary or the separatrix (the red dashed line in Fig. 2). The amplitude of the vacuum RMP field is linearly increased from zero to maximum with a build-up time of $200 \tau_A$ and then remains constant until

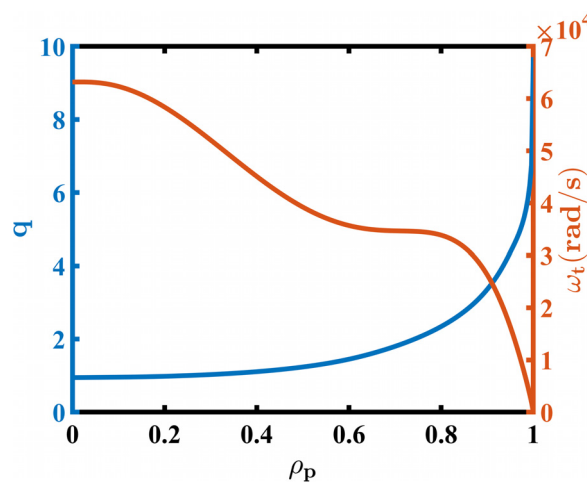


FIG. 1. Initial profiles of the safety factor q and the toroidal rotation ω_t for EAST discharge 52340.

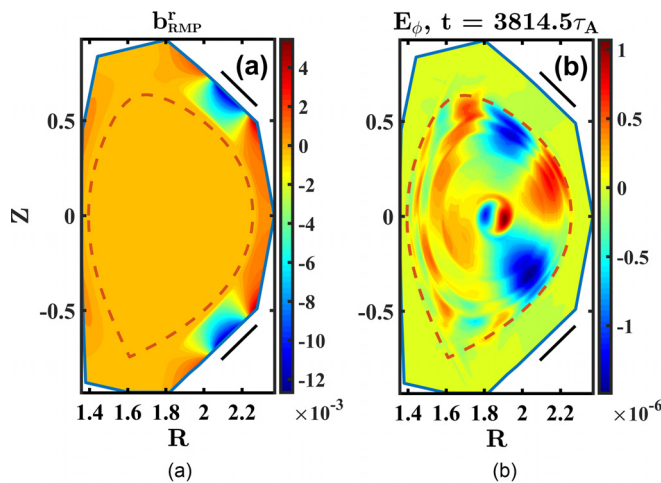


FIG. 2. (a) Initial b'_{RMP} distribution in the $\Phi = 0$ plane for RMP (10 kAt, $n = 1$, $\Delta\Phi = 0$). The initial RMP field fills the SOL but rapidly decreases to zero before reaching the plasma boundary (the red dashed line). (b) The toroidal electric field E_ϕ from CLTx at the saturated stage when magnetic field lines become chaotic at the pedestal. The blue solid line demarcates the simulation boundary. A pair of upper (U) and low (L) RMP coils are plotted with two black bars.

the end of the simulation. At the simulation boundary (the blue solid line in Fig. 2), the magnetic field is chosen to be the superposition of the initial equilibrium field and the vacuum RMP field, and all the other variables are fixed. In the linear simulation, the linear mode coupling associated with the toroidal effect is still retained although the nonlinear terms in MHD equations are dismissed.

In this work, the PEST coordinate,⁴⁴ i.e., the basic straight field line coordinate (ρ_p , θ , ϕ)⁴⁵ is used for spectrum analysis. ρ_p is the square root of the normalized poloidal flux ψ_p . The generalized poloidal angle θ is obtained by tracing field lines⁹ (θ in the SOL is extrapolated from the nearest point at the plasma boundary), and the toroidal angle ϕ is chosen to be its spatial value.

B. Plasma response to the $n=1$ RMP

In this subsection, we study the $n = 1$ RMP without a phase difference between the upper and low RMP coils ($\Delta\Phi = 0$). The total current in each RMP coil is set to the experimental value of 10 kAt. The Spitzer resistivity is also chosen to be the experimental value, $\eta_0 = 5 \times 10^{-9}$. A relative dense mesh of $512 \times 32 \times 512$ in (R, ϕ, Z) is used in this simulation. As shown in Fig. 2(b) from CLTx, the toroidal electric field E_ϕ induced by RMP is clearly separated by the rational surfaces at the saturated stage.⁴⁶ A remarkable $m/n = 1/1$ kink mode is found in the plasma core.

Without the plasma response or in vacuum, the resulting magnetic field can be calculated by the superposition of the initial equilibrium field and the vacuum RMP field. The $m/n = 3/1$ island is clear with a considerable width as shown in Fig. 3(a). In the region $\rho_p > 0.90$, magnetic field lines become chaotic because islands at different rational surfaces are large enough to overlap with each other. However, with the plasma response, the Poincaré plot of magnetic field lines from CLTx is shown in Fig. 3(b) at the saturated stage. It is evident that the widths of magnetic islands at all rational surfaces are substantially reduced. Specifically, the $m/n = 3/1$ island is almost invisible due to plasma shielding. Correspondingly, the chaotic region becomes much narrower ($\rho_p > 0.97$) than that in vacuum ($\rho_p > 0.90$). At high rational surfaces ($q > 6$), due to a large resistivity (associated with low plasma temperature) and weak toroidal rotation at the plasma edge, the plasma shielding is relatively weak and the island widths become comparable with those in vacuum.

The $b'_{n=1}$ spectra in vacuum and with a plasma response are given in Fig. 4. Along the resonant curve where $m = nq$, the magnetic field perturbations at rational surfaces are significantly weakened after considering the plasma response, although a bit of nonresonant amplification is found in Fig. 4(b). Through a careful comparison, it is found that the island widths, the edge stochasticity, the resonant shielding, and the nonresonant amplification from CLTx are in good agreement with those from MARS-F in Ref. 37. The reason for the good agreement between two codes for the $n = 1$ RMP is that in the low resistivity regime, magnetic field perturbations at rational surfaces will not

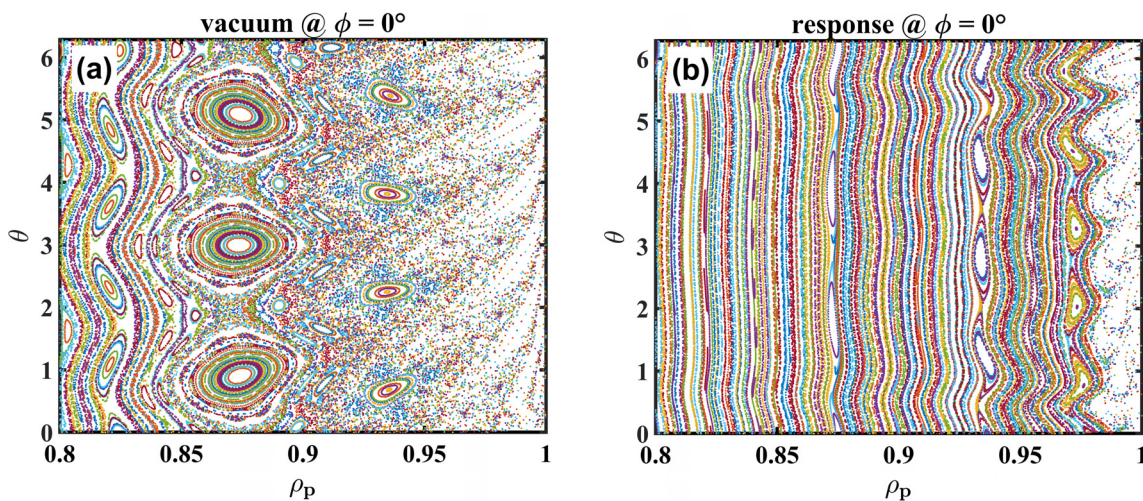


FIG. 3. Poincaré plots of magnetic field lines in vacuum (a) and with a plasma response (b) from CLTx.

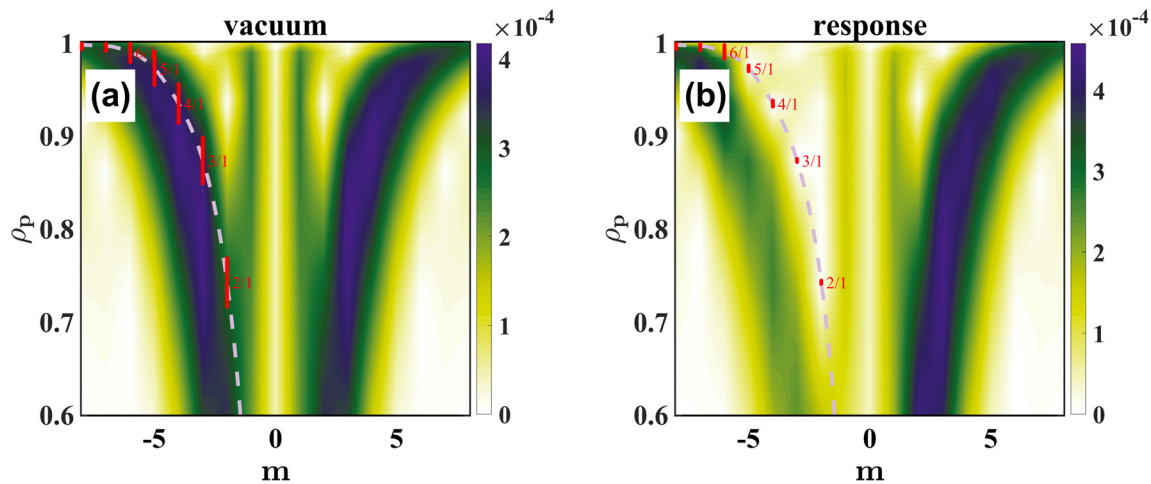


FIG. 4. Spectra of $b'_{h=1}$ in vacuum (a) and with a plasma response (b) from CLTx. The magnetic island width at each rational surface is indicated with the red line, and the dashed line represents the resonant curve where $m = nq$.

grow to large enough to destroy the magnetic flux surfaces in our simulation, which means that the assumption of the perturbative model in MARS-F is still valid.

We also conduct a set of linear simulations with and without including toroidal rotation. A larger resistivity of $\eta_0 = 5 \times 10^{-7}$ is used in this set of comparison simulations. The time evolutions of resonant harmonics $b'_{m/n}$ at different rational surfaces are given in Fig. 5. It is found that without toroidal rotation, the magnetic island with the plasma response exhibits a normal linear growth without saturation as shown in Fig. 5(b). It is well known that without toroidal rotation, all modes are locked with RMP. Therefore, RMP continuously drives modes to grow without saturation, which is significantly different from that with the toroidal rotation, where the magnetic island at high

rational surfaces ($q > 1$) reaches the saturated level⁴⁶ as shown in Fig. 5(a), though the inside unstable $m/n = 1/1$ kink mode still shows a linear growth. The plasma response with toroidal rotation plays the screening role in RMP penetration, which is qualitatively consistent with results of MARS-F.¹⁵ Because the Hall term is still missing in this study, the screening effect from toroidal rotation is contributed by the thermal ion flow, rather than the perpendicular electron flow as demonstrated by the two-fluid model used in JOREK²³ and M3D-C1.¹⁶ Since the pressure gradient at the pedestal is large and the two-fluid effect could be crucial in influencing the RMP penetration, a systematic study on the screening effect from toroidal rotation and perpendicular electron flow will be carried out in the next work by including both the toroidal rotation profile and Hall term in CLTx.

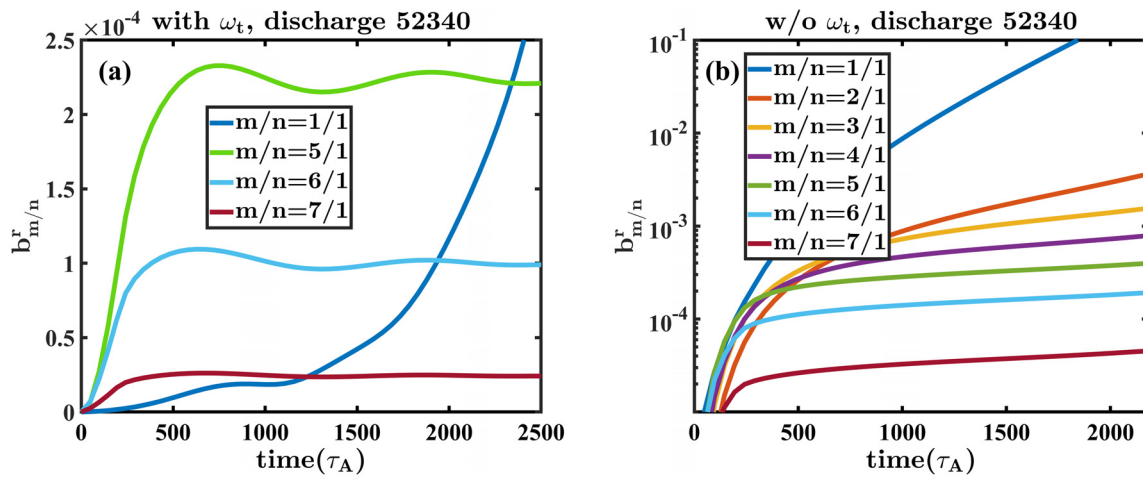


FIG. 5. Time evolutions of resonant harmonics $b'_{m/n}$ at different rational surfaces from linear simulations of CLTx for discharge 52340, with toroidal rotation (a) and without toroidal rotation (b). Note that the magnitude of the $m/n = 1/1$ harmonic in (a) is reduced by multiplying a factor of 0.02. A larger resistivity of $\eta_0 = 5 \times 10^{-7}$ is used in this set of comparison simulations. The vertical axis is set to be linear in (a), but logarithmic in (b).

C. Effect of $\Delta\Phi$ on resonant harmonics at $q=7$ rational surface

Experimental and MARS-F results¹⁴ indicate that the phase difference $\Delta\Phi$ between the upper and low RMP coils is a crucial parameter for ELM suppression or mitigation. We carry out a systematic simulation to investigate how $\Delta\Phi$ affects the RMP penetration with the plasma response in the pedestal region. The previous research^{14,42} suggested that the optimal ELM suppression or mitigation is achieved when the total resonant harmonic $b'_{m,n}$ with the plasma response has the maximum value at the last rational surface. MARS-F and experimental results on scanning $\Delta\Phi$ indicate that there exists an offset of the optimal coil phase difference $\Delta\Phi_{opt}$ in vacuum and with the plasma response.^{14,42} For instance, the $\Delta\Phi_{opt}$ in vacuum for $n=1$ RMP in EAST 52340 discharge is 315° , while with the plasma response, that value from MARS-F becomes 15° , which is also supported by experiment.¹⁴

A notable difference between CLTx and MARS-F is that for MARS-F, the X-point in the EFIT equilibrium is removed by smoothing the magnetic flux in the vicinity of the X-point to obtain a finite q value at the separatrix or the plasma boundary ($q_{max} = 7$ for discharge 52340),¹⁴ while in CLTx, the X-point is retained naturally and q is not able to be determined at the separatrix. Thus, we choose the resonant harmonic at the $q=7$ surface in CLTx for comparison with MARS-F.

Figure 6 shows the amplitudes of resonant harmonics vs $\Delta\Phi$ for $n=1$ and $n=2$ RMP at the $q=7$ rational surface. It is evident that the optimal coil phase difference $\Delta\Phi_{opt}$ corresponding to the maximum $b'_{m/n=7/1}$ for $n=1$ in vacuum is about 315° , while with the plasma response, $\Delta\Phi_{opt}$ is less than 45° from CLTx, which is consistent with the MARS-F result, where $\Delta\Phi_{opt}$ equals to 315° in vacuum, and 15° with the plasma response [see dashed arrows in Fig. 6(a)], and the detailed results of MARS-F could be found in Fig. 3(a) of Ref. 14]. For the $n=2$ RMP, $\Delta\Phi_{opt}$ giving the maximum $b'_{m/n=14/2}$ is 270° in vacuum and 0° with plasma response from CLTx, respectively, which is different from that of MARS-F, where $\Delta\Phi_{opt}$ equals to 195° in

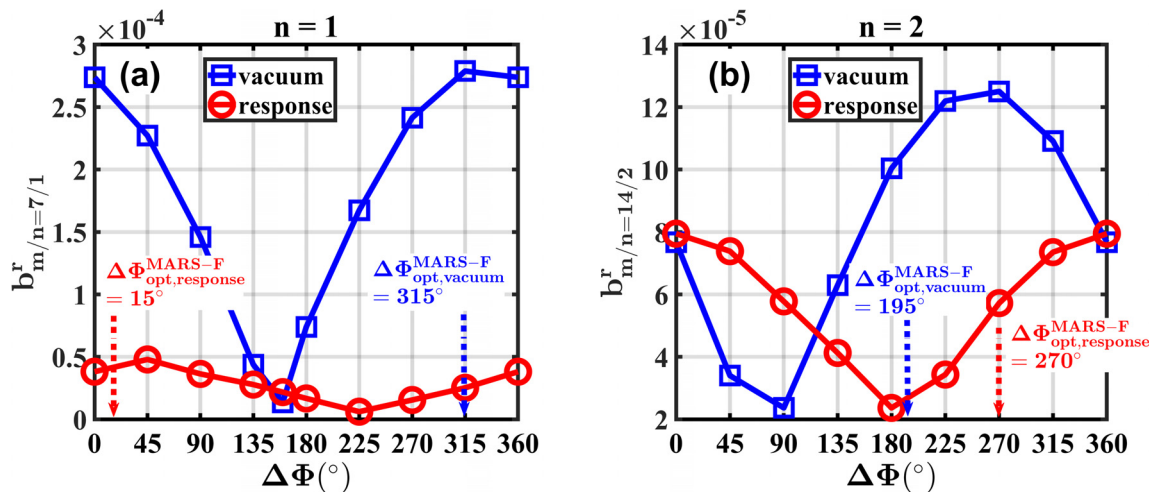


FIG. 6. Amplitudes of resonant harmonics at the $q=7$ rational surface vs the phase difference between the upper and low coils, $\Delta\Phi$, for $n=1$ (a) and $n=2$ (b) RMP from CLTx. The resonant field strengths in vacuum and with the plasma response are indicated by blue squares and red circles, respectively. The total resonant field with the plasma response results from both the RMP field in vacuum and the induction field due to the plasma response. $\Delta\Phi_{opt}$ of MARS-F calculations¹⁴ are marked out with dashed arrows for resonant harmonics in vacuum (blue) and with the plasma response (red), respectively.

vacuum and 270° with the plasma response [see dashed arrows in Fig. 6(b)], and the detailed results of MARS-F could be found in Fig. 3(b) of Ref. 14].

The $\Delta\Phi_{opt}$ difference between CLTx and MARS-F for the $n=2$ RMP could result from retaining the X-point in CLTx. With the presence of the X-point and the SOL in CLTx, determining the generalized poloidal angle θ near the X-point and the plasma boundary by tracing field lines is difficult. Thus, diagnostics based on the straight field-line coordinate in the vicinity of the plasma boundary become inaccurate for high harmonic modes due to the short wavelengths. Beyond that, magnetic field perturbations in the SOL will propagate away from the system along opened magnetic field lines by shear Alfvén waves. Because the phase shift depends on the wavelength during propagations of magnetic field perturbations along opened field lines, a higher harmonic mode will lead to a larger phase shift in the SOL. Since we are not able to give accurate diagnoses of the $n=2$ harmonic mode in CLTx, we only focus on studying the $n=1$ RMP penetration for discharge 52340 at present.

IV. INFLUENCE OF THE RESISTIVITY FOR THE $n=1$ RMP PENETRATION

The influence of $\Delta\Phi$ between the upper and low RMP coils on the penetration of the $n=1$ RMP is further studied with different resistivities η_0 from 5×10^{-10} to 5×10^{-7} . The offset of $\Delta\Phi_{opt}$ in vacuum and with the plasma response decreases with increasing the resistivity as shown in Fig. 7. For the case with $\eta_0 = 5 \times 10^{-10}$, $\Delta\Phi_{opt}$ is about 90° with the plasma response and 315° in vacuum. Thus, there is a 135° offset for $\Delta\Phi_{opt}$ in vacuum and with the plasma response. When the resistivity increases to $\eta_0 = 5 \times 10^{-7}$, the offset for $\Delta\Phi_{opt}$ reduces to less than 45° . We also find that the amplitudes of the penetrated $m/n=7/1$ harmonics also increase with increasing the resistivity. For the large resistivity case $\eta_0 = 5 \times 10^{-7}$, the maximum resonant amplitude with the plasma response is almost identical to

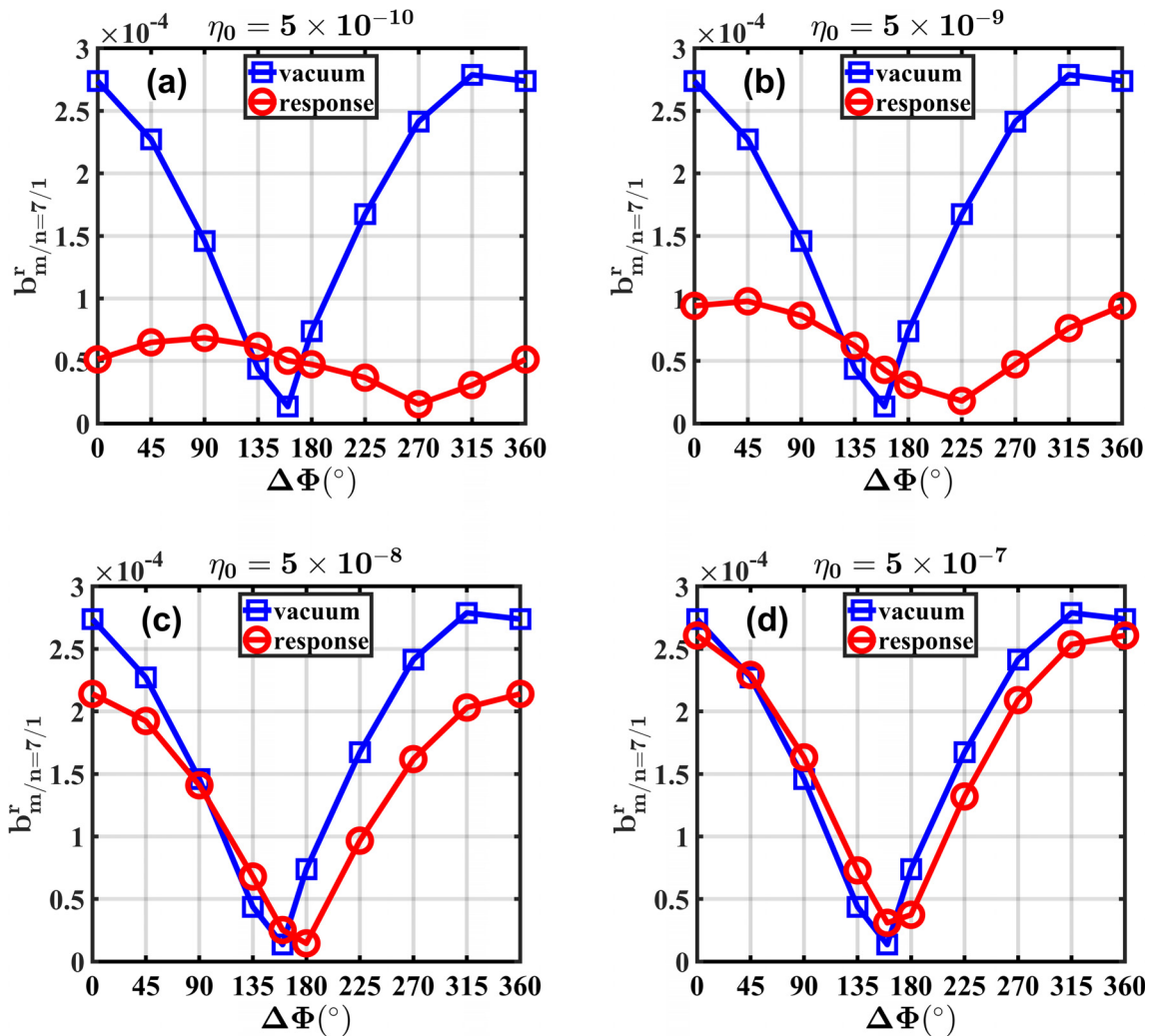


FIG. 7. Amplitudes of the $m/n = 7/1$ harmonics for the $n = 1$ RMP at the $q = 7$ rational surface with different resistivities (blue squares in vacuum and red circles for the total resonant fields with the plasma response).

that in vacuum, which suggests that the screening effect could disappear with a larger resistivity.

Figure 8 shows the phase angles $\phi_{m/n}$ for the $m/n = 8/1$ and $7/1$ resonant harmonics with the resistivity $\eta_0 = 5 \times 10^{-10}$ and 5×10^{-7} . The antiphase regimes (where the phase difference $\delta\phi_{m/n}$ between the RMP field for the vacuum and the total resonant fields with the plasma response is π) are shaded light blue. With small resistivity $\eta_0 = 5 \times 10^{-10}$, the phases $\phi_{m/n}$ for both $m/n = 8/1$ and $7/1$ total resonant fields with the plasma response are quite different from those in vacuum. Specifically, the phase difference $\delta\phi_{m/n}$ in vacuum and with plasma response is almost π in the regimes of $180^\circ < \Delta\Phi < 315^\circ$ for $m/n = 8/1$ and $135^\circ < \Delta\Phi < 270^\circ$ for $m/n = 7/1$, which results in the distinct discrepancies of the resonant field amplitudes in vacuum and with the plasma response. As we know, with the plasma response, the $m/n = 7/1$ total resonant field at the $q = 7$ rational surface results from the $m/n = 7/1$ component of vacuum RMP and the $m/n = 8/1$ resonant field with the plasma response at the $q = 8$ rational surface due to

the toroidal coupling effect. Since the total $m/n = 7/1$ resonant field with the plasma response is much larger than that in vacuum at $\Delta\Phi = 160^\circ$ as shown in Fig. 6(a), it is suggested that the $m/n = 8/1$ resonant field at the $q = 8$ rational surface makes a major contribution, which is confirmed by Figs. 8(a) and 8(b), where the phases for the $m/n = 7/1$ and $8/1$ resonant fields with the plasma response are the same, but the $m/n = 7/1$ harmonics in vacuum and with the plasma response are antiphase. Similarly, for $\Delta\Phi = 270^\circ$, the phases of the $m/n = 7/1$ harmonic in vacuum and the $m/n = 8/1$ total resonant field with the plasma response are almost antiphase, which suggests that contributions on the $m/n = 7/1$ component directly from the vacuum RMP and indirectly from the $m/n = 8/1$ total resonant field with the plasma response due to toroidal coupling have the opposite phases and nearly the same amplitudes. The antiphase cancellation of these two opposite contributions leads to the lowest amplitude of the $m/n = 7/1$ total resonant field with the plasma response at $\Delta\Phi = 270^\circ$ as shown in Fig. 7(a).

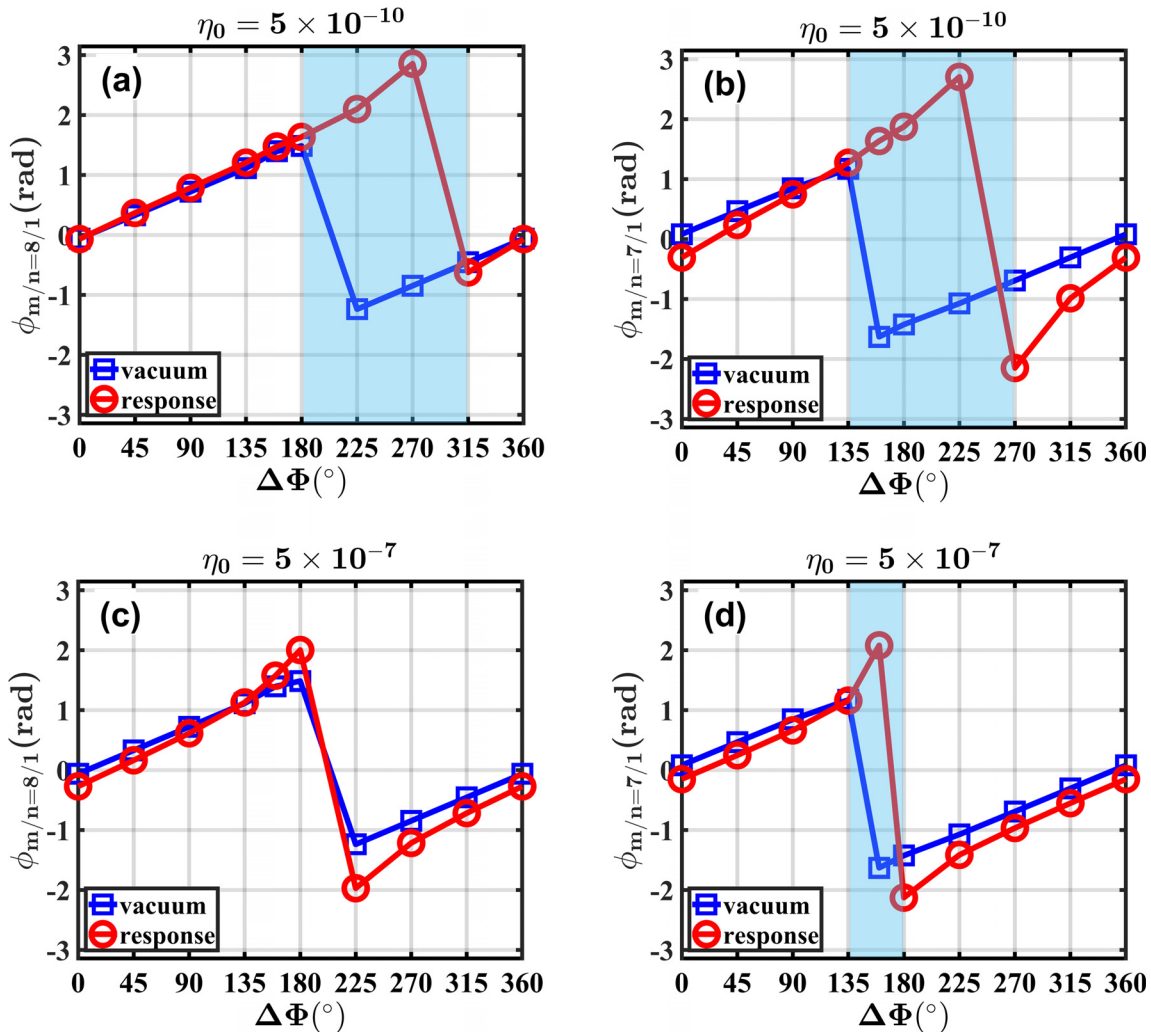


FIG. 8. The phase angles $\phi_{m/n}$ (ranging from $-\pi$ to π) of resonant harmonics at rational surfaces with $q=8$ (left column) and $q=7$ (right column) for the resistivity $\eta_0 = 5 \times 10^{-10}$ (top panel) and $\eta_0 = 5 \times 10^{-7}$ (low panel). The antiphase regimes (where the phase difference $\delta\phi_{m/n}$ between the RMP field for the vacuum and the total resonant fields with plasma response is π) are shaded light blue.

In contrast, with a larger resistivity $\eta_0 = 5 \times 10^{-7}$, the phase difference of the $m/n = 8/1$ harmonic in vacuum and with the plasma response almost disappears as given in Fig. 8(c). Only a very narrow antiphase regime can be found for the $m/n = 7/1$ harmonic around $\Delta\Phi = 160^\circ$ in Fig. 8(d), which results from the toroidal coupling contribution from $m/n = 8/1$ resonant harmonic with the plasma response as explained above. The small phase shift of resonant harmonics in vacuum and with the plasma response for a large resistivity suggests that the screen current induced by RMP is greatly reduced due to large resistive diffusion in plasma. It implies that the toroidal coupling effect is very important when considering the plasma response in the low resistivity regime.

It is also noticed that the phase shift $\delta\phi_{m/n}$ in vacuum and with the plasma response in Fig. 8 is either π (antiphase) or 0 (inphase), which is quite different from either $\pi/2$ or 0 phase shift reported in previous studies.^{47–49} The $\pi/2$ phase shift with the plasma response

arises mainly due to generation of a screen current with low resistivity,^{48,49} which is similar to the shift of the $m/n = 3/1$ and $4/1$ islands from CLTx in Figs. 3(a) and 3(b).³⁷ For the resonant harmonics of $m/n = 7/1$ and $8/1$, the corresponding rational surfaces are quite close to the plasma boundary where the resistivity is high and the toroidal rotation speed is low. Consequently, the screen current is easily dissipated at high rational surfaces, which results in the absence of a $\pi/2$ phase shift in Fig. 8.

To understand the physical mechanisms of the phase shift $\delta\phi_{m/n}$ and the offset in $\Delta\Phi_{opt}$, the distributions of radial magnetic perturbations b_{RMP}^r for RMP with $\Delta\Phi = 0$ in vacuum and with the plasma response are given in Fig. 9. The propagation or the amplitude descent directions of b_{RMP}^r at the two primary perturbed petals (the regions with the deep blue color closing to the RMP coils) are marked out with black arrows for each case. The solid arrows in Fig. 9 indicate the radially inward propagations, while the dotted arrows in Fig. 9(b)

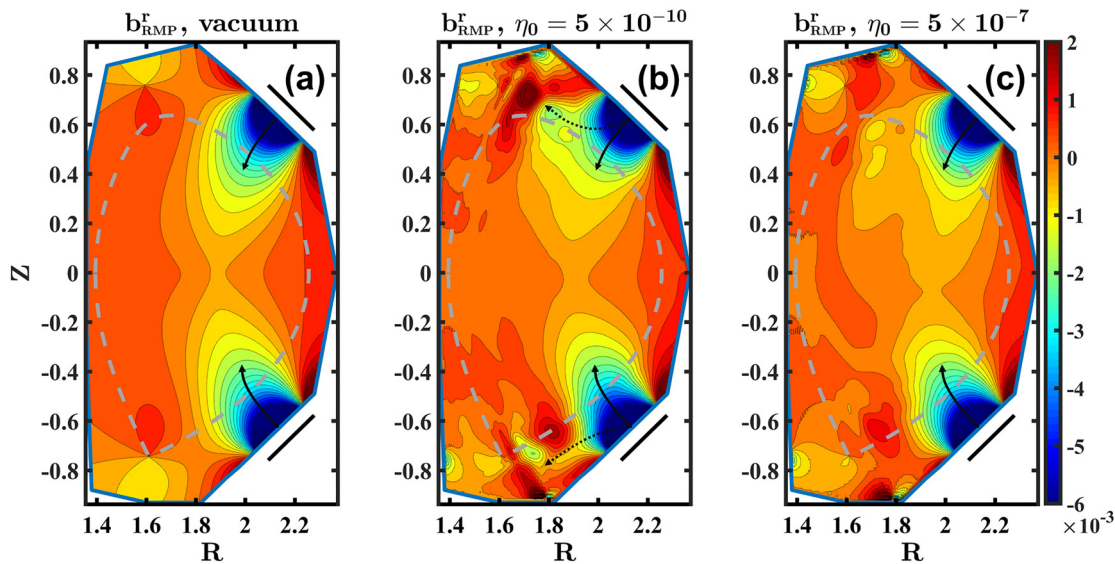


FIG. 9. Distributions of radial magnetic perturbations b_{RMP}^r in vacuum (a) and with the plasma response for $\eta_0 = 5 \times 10^{-10}$ (b) and $\eta_0 = 5 \times 10^{-7}$ (c). The propagation or the amplitude descent directions of b_{RMP}^r at the two primary perturbed petals (the regions with the deep blue color closing to the RMP coils) are marked out with black arrows for each case. The solid arrows indicate the radially inward propagations, while the dotted arrows in (b) indicate the poloidal propagations of RMP along opened field lines in the SOL.

indicate the poloidal propagations of RMP along opened field lines in the SOL. For the case with a lower resistivity ($\eta_0 = 5 \times 10^{-10}$), it takes a longer time for magnetic field perturbation to be diffused and to reach the plasma boundary or the separatrix. The lower dissipation on the screen current at rational surfaces also contributes to a longer time scale for establishing a steady state. As a result, except for the radial penetration indicated by the solid arrows, the magnetic perturbation in the SOL exhibits poloidal propagations along opened magnetic field lines at the low field side (LFS) [see dotted arrows in Fig. 9(b)]. The shift directions for the upper and low petals are, respectively, upward and downward, which indicates that magnetic perturbation has propagated away along opened field lines. However, for a large resistivity ($\eta_0 = 5 \times 10^{-7}$), the time scale of the radial diffusion in the SOL is shorter and there is no larger screen current building up at rational surfaces, which results in a quick penetration of RMP and absence of the phase shift in the SOL. Thus, the propagation directions in Fig. 9(c) are mainly radially inward as indicated by the solid arrows, which is almost the same as that in vacuum as shown in Fig. 9(a).

To distinguish the roles of resistivity in the SOL and plasma region, a supplementary set of simulations for the $n=1$ RMP is carried out by artificially increasing the resistivity in the SOL by three orders of magnitude. Thus, the resistivity is $\eta_0 = 5 \times 10^{-10}$ inside the last closed surface and it is $\eta_0 = 5 \times 10^{-7}$ in the SOL. The amplitudes and phases of resonant fields at the $q=7$ rational surface vs $\Delta\Phi$ are given in Fig. 10. In comparison with the previous results in Figs. 7(a) and 8(b) (where the resistivity is $\eta_0 = 5 \times 10^{-10}$ in the SOL), it is found that with larger resistivity in the SOL, the offset of $\Delta\Phi_{opt}$ in vacuum and with the plasma response almost disappears and the amplitudes of total resonant fields with the plasma response increase as shown in Fig. 10(a). Meanwhile, the obvious phase difference $\delta\phi_{m/n}$ of π observed in Fig. 8(b) for resonant harmonics at $q=7$ rational surface almost vanishes as well in Fig. 10(b). Only a very narrow

antiphase regime shaded light blue is observed, which is also attributed to the toroidal coupling effect of $m/n=8/1$ resonant harmonic with plasma response as demonstrated above.

Besides that, an opposite setup of the resistivity distribution, (i.e., the resistivity is $\eta_0 = 5 \times 10^{-7}$ inside the last closed surface while it is $\eta_0 = 5 \times 10^{-10}$ in the SOL) has been carried out as well. The results are given in Fig. 11. With this opposite resistivity distribution, the amplitudes and phases of resonant fields at the $q=7$ rational surface vs $\Delta\Phi$ are quite similar to those in Figs. 7(a) and 8(b) as we expected. Therefore, this supplementary study of the two resistivity distributions suggests that the results strongly depend on the resistivity in the SOL in cases with retaining the SOL and the X-point. The low resistivity in the SOL results in phase shifts of the total resonant field at the rational surface with plasma response, even though the resistivity inside the last closed surface is large. But the results with the high resistivity in the SOL appear to be opposite.

With $\eta_0 = 5 \times 10^{-10}$ inside the last closed surface, we further conducted other two cases with $\eta_0 = 5 \times 10^{-9}$ and $\eta_0 = 5 \times 10^{-8}$ in the SOL. It is found that for the case with $\eta_0 = 5 \times 10^{-9}$ in SOL, the result from CLTx in Fig. 12(a) is still in good agreement with that of $\eta_0 = 5 \times 10^{-10}$ in the SOL as shown in Fig. 7(a), while for the case with $\eta_0 = 5 \times 10^{-8}$, the result in Fig. 12(b) is evidently deviated from that in Fig. 7(a). Therefore, the adjustment or the choice of the SOL resistivity within the experimental parameter range (less than one order of magnitude) should not influence the benchmark results between CLTx and MARS-F.

The SOL and the X-point retaining in CLTx result in a phase shift for high m mode inside the plasma boundary in cases with a low resistivity in the SOL. Due to opened magnetic field lines in the SOL, the imposed magnetic perturbation tends to propagate along field lines by shear Alfvén waves. The magnetic field perturbation will reach a steady state in the SOL after a time period that is mainly determined

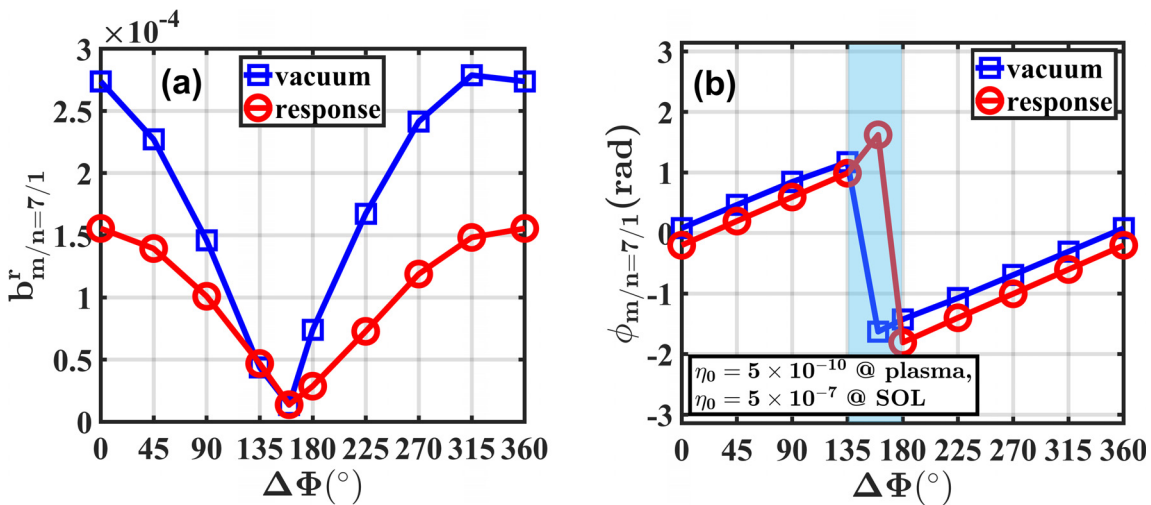


FIG. 10. Amplitudes (a) and phases (b) of resonant harmonics at the $q=7$ rational surface vs $\Delta\Phi$, for the $n=1$ RMP (blue squares in vacuum and red circles for the total resonant fields with plasma response). The resistivity inside the last closed surface is $\eta_0 = 5 \times 10^{-10}$, but in the SOL it is set to be three orders of magnitude larger, i.e., $\eta_0 = 5 \times 10^{-7}$. The antiphase regime (where the phase difference $\delta\phi_{m/n=7/1}$ of resonant fields in vacuum and with the plasma response is π) is shaded light blue.

by the radial diffusion time of the magnetic field or the resistivity. Therefore, with the lower resistivity, the shear Alfvén wave carries more energy of the magnetic perturbation away from the system in the SOL. Along with the dependence of the screen current,⁴⁸ the amplitude reduction and the phase shift of the total resonant field increase with decreasing the resistivity. It also explains why the reduction and the phase shift also depend on the mode number because the phase shift associated with the propagation of the magnetic field perturbation is related to the mode wavelength. Therefore, in CLTx simulations, the phase shifts and the amplitudes of total resonant field with the plasma response for a low resistivity are simultaneously determined by the direct contribution of the corresponding harmonic in

vacuum RMP and the indirect contribution of the total resonant field at the outer neighboring rational surface due to the toroidal coupling effect.

Since a rational surface can prevent a resonant mode from penetrating, the mode inside the rational surface is not directly penetrated by the same harmonic in vacuum RMP, instead influenced by the mode coupling due to toroidal effect. For instance, in the above discussion, the amplitude and the phase of the $m/n=7/1$ total resonant field with the plasma response strongly depend on the adjacent resonant harmonic of $m/n=8/1$, rather than the vacuum RMP field. Similarly, the resonant field at a lower $q=6$ rational surface has a similar dependence on the $m/n=7/1$ resonant

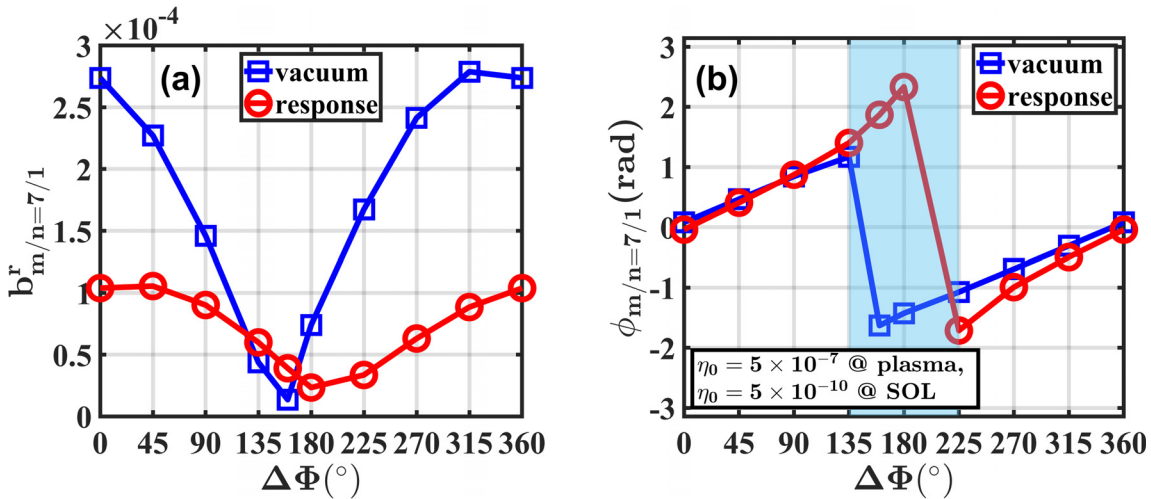


FIG. 11. Amplitudes (a) and phases (b) of resonant harmonics at the $q=7$ rational surface vs $\Delta\Phi$, for the $n=1$ RMP (blue squares in vacuum and red circles for the total resonant fields with the plasma response). The resistivity inside the last closed surface is $\eta_0 = 5 \times 10^{-7}$, but in the SOL it is set to be three orders of magnitude smaller, i.e., $\eta_0 = 5 \times 10^{-10}$. The antiphase regime (where the phase difference $\delta\phi_{m/n=7/1}$ of resonant fields in vacuum and with plasma response is π) is shaded with light blue.

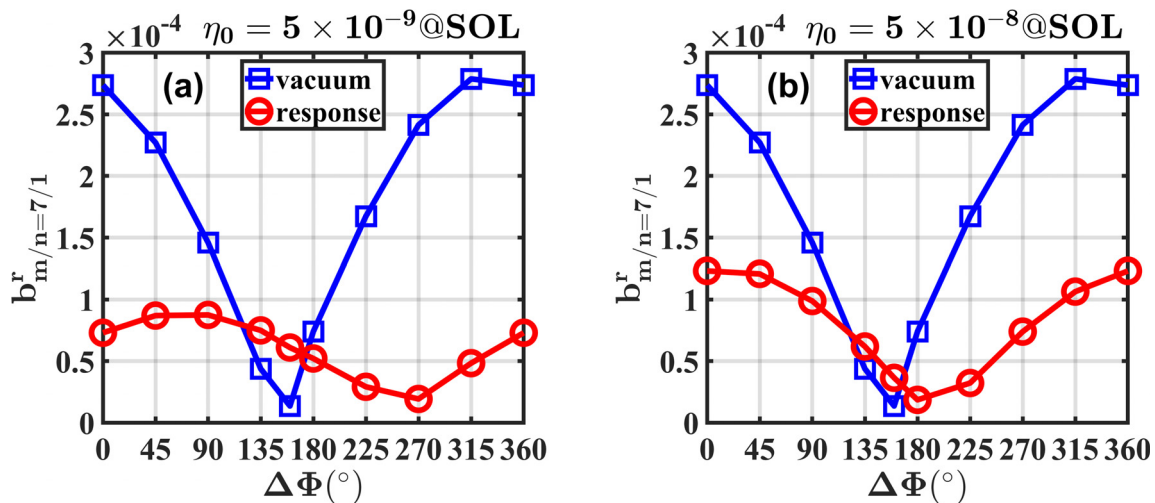


FIG. 12. Amplitudes of the $m/n = 7/1$ harmonics for the $n = 1$ RMP at the $q = 7$ rational surface with (a) $\eta_0 = 5 \times 10^{-9}$ and (b) $\eta_0 = 5 \times 10^{-8}$ in the SOL, respectively. The resistivity inside the last closed surface is $\eta_0 = 5 \times 10^{-10}$.

harmonic, and so on. In consequence, the figure of merit (FoM) based on the amplitude of resonant harmonics at the last rational surface could relatively reflect the island overlapping for multiple rational surfaces at the pedestal and further affect the optimal coil difference $\Delta\Phi_{opt}$ for best ELM control.¹⁴

V. CONCLUSION AND DISCUSSION

CLT is upgraded to CLTx for including the SOL with new boundary handling method, GPU-acceleration, and the RMP modules. For ELM mitigation discharge 52340 in EAST, the linear simulation results with the experimental parameters and RMP configurations from CLTx are in good agreement with those from MARS-F. Specifically, the optimal coil differences $\Delta\Phi_{opt}$ for the $n = 1$ RMP are almost the same.

The simulation results with different resistivities suggest that the amplitude reduction and the phase shift of the total resonant field increase with decreasing the resistivity when they reach the plasma boundary. A phase shift of π in vacuum and with the plasma response is observed, which is quite different from the $\pi/2$ shift due to the presence of screen current.^{48,49} The strong phase dependency between adjacent rational surfaces indicates that the toroidal coupling effect is important in studying RMP with plasma response. The phase shift of RMP in the SOL appears in the regime with low resistivity, and it vanishes with increasing resistivity. The amplitude reduction and the phase shift also depend on the mode number because the mode phase shift due to the propagation of the magnetic field perturbation along opened field lines is related to the mode wavelength.

ACKNOWLEDGMENTS

The authors would like to acknowledge helpful suggestions given by Professor W. W. Xiao and Dr. Q. Wang. This work was supported by the National Natural Science Foundation of China under Grant Nos. 11775188 and 11835010, the Special Project on High-performance Computing under the National Key R&D Program of China No. 2016YFB0200603, and Fundamental Research Fund for Chinese Central Universities.

REFERENCES

- ¹H. Zohm, *Plasma Phys. Controlled Fusion* **38**(2), 105–128 (1996).
- ²F. Wagner, G. Becker, K. Behringer, D. Campbell, A. Eberhagen, W. Engelhardt, G. Fussmann, O. Gehre, J. Gernhardt, G. v Gierke, G. Haas, M. Huang, F. Karger, M. Keilhacker, O. Klüber, M. Kornherr, K. Lackner, G. Lisitano, G. G. Lister, H. M. Mayer, D. Meisel, E. R. Müller, H. Murmann, H. Niedermeyer, W. Poschenrieder, H. Rapp, H. Röhr, F. Schneider, G. Siller, E. Speth, A. Stäbler, K. H. Steuer, G. Venus, O. Vollmer, and Z. Yü, *Phys. Rev. Lett.* **49**(19), 1408–1412 (1982).
- ³T. Evans, M. Fenstermacher, R. Moyer, T. Osborne, J. Watkins, P. Gohil, I. Joseph, M. Schaffer, L. R. Baylor, and M. Bécoulet, *Nucl. Fusion* **48**(2), 024002 (2008).
- ⁴Y. Liang, H. R. Koslowski, P. R. Thomas, E. Nardon, B. Alper, P. Andrew, Y. Andrew, G. Arnoux, Y. Baranov, M. Bécoulet, M. Beurskens, T. Biewer, M. Bigi, K. Crombe, E. De La Luna, P. de Vries, W. Fundamenski, S. Gerasimov, C. Giroud, M. P. Gryaznevich, N. Hawkes, S. Hotchin, D. Howell, S. Jachmich, V. Kiptily, L. Moreira, V. Parail, S. D. Pinches, E. Rachlew, and O. Zimmermann, *Phys. Rev. Lett.* **98**(26), 265004 (2007).
- ⁵A. Kirk, J. Harrison, Y. Liu, E. Nardon, I. T. Chapman, and P. Denner, *Phys. Rev. Lett.* **108**(25), 255003 (2012).
- ⁶W. Suttrop, T. Eich, J. C. Fuchs, S. Günter, A. Janzer, A. Herrmann, A. Kallenbach, P. T. Lang, T. Lunt, M. Maraschek, R. M. McDermott, A. Mlynek, T. Pütterich, M. Rott, T. Vierle, E. Wolfrum, Q. Yu, I. Zammuto, and H. Zohm (ASDEX Upgrade Team), *Phys. Rev. Lett.* **106**(22), 225004 (2011).
- ⁷W. W. Xiao, T. E. Evans, G. R. Tynan, S. W. Yoon, Y. M. Jeon, W. H. Ko, Y. U. Nam, Y. K. Oh, and K. Team, *Phys. Rev. Lett.* **119**(20), 205001 (2017).
- ⁸Y. Sun, Y. Liang, Y. Liu, S. Gu, X. Yang, W. Guo, T. Shi, M. Jia, L. Wang, and B. Lyu, *Phys. Rev. Lett.* **117**(11), 115001 (2016).
- ⁹M. Bécoulet, E. Nardon, G. Huysmans, W. Zwingmann, P. Thomas, M. Lipa, R. Moyer, T. Evans, V. Chuyanov, and Y. Gribov, *Nucl. Fusion* **48**(2), 024003 (2008).
- ¹⁰Z. Ma, X. Wang, and A. Bhattacharjee, *Phys. Plasmas* **3**(6), 2427–2433 (1996).
- ¹¹X. Wang, Z. Ma, and A. Bhattacharjee, *Phys. Plasmas* **3**(5), 2129–2134 (1996).
- ¹²A. H. Boozer and C. Nührenberg, *Phys. Plasmas* **13**(10), 102501 (2006).
- ¹³A. H. Boozer, *Phys. Plasmas* **13**(4), 044501 (2006).
- ¹⁴X. Yang, Y. Sun, Y. Liu, S. Gu, Y. Liu, H. Wang, L. Zhou, and W. Guo, *Plasma Phys. Controlled Fusion* **58**(11), 114006 (2016).
- ¹⁵L. Li, Y. Liu, Y. Liang, N. Wang, Q. Luan, F. Zhong, and Y. Liu, *Nucl. Fusion* **56**(9), 092008 (2016).
- ¹⁶M. R. Wade, R. Nazikian, T. Evans, N. Ferraro, R. Moyer, D. Orlov, R. Butterly, M. Fenstermacher, A. Garofalo, and M. Lanctot, *Nucl. Fusion* **55**(2), 023002 (2015).

- ¹⁷A. Wingen, N. M. Ferraro, M. W. Shafer, E. A. Unterberg, J. M. Canik, T. E. Evans, D. L. Hillis, S. P. Hirshman, S. K. Seal, and P. B. Snyder, *Plasma Phys. Controlled Fusion* **57**(10), 104006 (2015).
- ¹⁸R. A. Moyer, C. Paz-Soldan, R. Nazikian, D. M. Orlov, N. Ferraro, B. A. Grierson, M. Knölker, B. Lyons, G. R. McKee, and T. H. Osborne, *Phys. Plasmas* **24**(10), 102501 (2017).
- ¹⁹E. Nardon, M. Bécoulet, G. Huysmans, and O. Czarny, *Phys. Plasmas* **14**(9), 092501 (2007).
- ²⁰F. Orain, M. Hoelzl, E. Viezzier, M. Dunne, M. Bécoulet, P. Cahyna, G. T. A. Huijsmans, J. Morales, M. Willensdorfer, and W. Suttrop, *Nucl. Fusion* **57**(2), 022013 (2017).
- ²¹F. Liu, G. Huijsmans, A. Loarte, A. M. Garofalo, W. M. Solomon, P. B. Snyder, M. Hoelzl, and L. Zeng, *Nucl. Fusion* **55**(11), 113002 (2015).
- ²²M. Bécoulet, F. Orain, G. Huijsmans, S. Pamela, P. Cahyna, M. Hoelzl, X. Garbet, E. Franck, E. Sonnendrücker, and G. Dif-Pradalier, *Phys. Rev. Lett.* **113**(11), 115001 (2014).
- ²³F. Orain, M. Bécoulet, G. Dif-Pradalier, G. Huijsmans, S. Pamela, E. Nardon, C. Passeron, G. Latu, V. Grandgirard, and A. Fil, *Phys. Plasmas* **20**(10), 102510 (2013).
- ²⁴V. A. Izzo and I. Joseph, *Nucl. Fusion* **48**(11), 115004 (2008).
- ²⁵A. Pankin, G. Bateman, D. Brennan, A. Kritz, S. Kruger, P. Snyder, and C. Sovinec and the NIMROD team, *Plasma Phys. Controlled Fusion* **49**(7), S63–S75 (2007).
- ²⁶W. Xiao, T. Evans, G. Tynan, and D. Eldon, *Nucl. Fusion* **56**(6), 064001 (2016).
- ²⁷T. E. Evans, R. A. Moyer, K. H. Burrell, M. E. Fenstermacher, I. Joseph, A. W. Leonard, T. H. Osborne, G. D. Porter, M. J. Schaffer, and P. B. Snyder, *Nat. Phys.* **2**(6), 419–423 (2006).
- ²⁸T. E. Evans, A. Loarte, D. M. Orlov, B. A. Grierson, M. M. Knölker, B. C. Lyons, L. Cui, P. Gohil, R. J. Groebner, R. A. Moyer, R. Nazikian, T. H. Osborne, and E. A. Unterberg, *Nucl. Fusion* **57**(8), 086016 (2017).
- ²⁹D. Yonghua, C. Zhongyong, C. Zhipeng, Y. Zhoujun, W. Nengchao, H. Qiming, R. Bo, C. Jie, Z. Cheng, and G. Li, *Plasma Sci. Technol.* **20**(12), 125101 (2018).
- ³⁰M. Lehnhen, S. A. Bozhenkov, S. S. Abdullaev, and M. W. Jakubowski (TEXTOR Team), *Phys. Rev. Lett.* **100**(25), 255003 (2008).
- ³¹M. Bécoulet, F. Orain, P. Maget, N. Mellet, X. Garbet, E. Nardon, G. T. A. Huijsmans, T. Casper, A. Loarte, P. Cahyna, A. Smolyakov, F. L. Waelbroeck, M. Schaffer, T. Evans, Y. Liang, O. Schmitz, M. Beurskens, V. Rozhansky, and E. Kaveeva, *Nucl. Fusion* **52**(5), 054003 (2012).
- ³²A. Rechester and M. Rosenbluth, *Phys. Rev. Lett.* **40**(1), 38 (1978).
- ³³S. Wang and Z. Ma, *Phys. Plasmas* **22**(12), 122504 (2015).
- ³⁴S. Wang, Z. Ma, and W. Zhang, *Phys. Plasmas* **23**(5), 052503 (2016).
- ³⁵W. Zhang, S. Wang, and Z. Ma, *Phys. Plasmas* **24**(6), 062510 (2017).
- ³⁶W. Zhang, Z. Ma, and S. Wang, *Phys. Plasmas* **24**(10), 102510 (2017).
- ³⁷Y. Sun, M. Jia, Q. Zang, L. Wang, Y. Liang, Y. Liu, X. Yang, W. Guo, S. Gu, and Y. Li, *Nucl. Fusion* **57**(3), 036007 (2017).
- ³⁸L. Duan, X. Wang, and X. Zhong, *J. Comput. Phys.* **229**(19), 7207–7237 (2010).
- ³⁹L. Lao, H. S. John, R. Stambaugh, A. Kellman, and W. Pfeiffer, *Nucl. Fusion* **25**(11), 1611 (1985).
- ⁴⁰H. Strauss, L. Sugiyama, G. Park, C. Chang, S. Ku, and I. Joseph, *Nucl. Fusion* **49**(5), 055025 (2009).
- ⁴¹H. W. Zhang, J. Zhu, Z. W. Ma, G. Y. Kan, X. Wang, and W. Zhang, “Acceleration of three-dimensional Tokamak magnetohydrodynamical code with graphics processing unit and OpenACC heterogeneous parallel programming,” *Int. J. Comput. Fluid Dyn.* (to be published); preprint arXiv:1812.00525.
- ⁴²Y. Liu, C. Ham, A. Kirk, L. Li, A. Loarte, D. Ryan, Y. Sun, W. Suttrop, X. Yang, and L. Zhou, *Plasma Phys. Controlled Fusion* **58**(11), 114005 (2016).
- ⁴³Y. Sun, Y. Liang, J. Qian, B. Shen, and B. Wan, *Plasma Phys. Controlled Fusion* **57**(4), 045003 (2015).
- ⁴⁴R. Grimm, R. Dewar, and J. Manickam, *J. Comput. Phys.* **49**(1), 94–117 (1983).
- ⁴⁵V. D. Pustovitov, *Plasma Phys. Rep.* **24**(6), 510–520 (1998).
- ⁴⁶N. Ferraro, *Phys. Plasmas* **19**(5), 056105 (2012).
- ⁴⁷Y. Sun, Y. Liang, K. C. Shaing, Y. Q. Liu, H. R. Koslowski, S. Jachmich, B. Alper, A. Alfier, O. Asunta, P. Buratti, G. Corrigan, E. Delabie, C. Giroud, M. P. Gryaznevich, D. Harting, T. Hender, E. Nardon, V. Naulin, V. Parail, T. Tala, C. Wiegmann, S. Wiesen, T. Zhang, and J.-E. Contributors, *Nucl. Fusion* **52**(8), 083007 (2012).
- ⁴⁸D. Reiser and D. Chandra, *Phys. Plasmas* **16**(4), 042317 (2009).
- ⁴⁹E. Kaveeva and V. Rozhansky, *Nucl. Fusion* **52**(5), 054011 (2012).